GALAXIES

# A magnified compact galaxy at redshift 9.51 with strong nebular emission lines

**Hayley Williams[1]*, Patrick L. Kelly[1], Wenlei Chen[1], Gabriel Brammer[2], Adi Zitrin[3], Tommaso Treu[4], Claudia Scarlata[1], Anton M. Koekemoer[5], Masamune Oguri[6,7], Yu-Heng Lin[1], Jose M. Diego[8], Mario Nonino[9], Jens Hjorth[10], Danial Langeroodi[10], Tom Broadhurst[11], Noah Rogers[1], Ismael Perez-Fournon[12,13], Ryan J. Foley[14], Saurabh Jha[15], Alexei V. Filippenko[16], Lou Strolger[5], Justin Pierel[5], Frederick Poidevin[12,13], Lilan Yang[17]**

Ultraviolet light from early galaxies is thought to have ionized gas in the intergalactic medium. However, there are few observational constraints on this epoch because of the faintness of those galaxies and the redshift of their optical light into the infrared. We report the observation, in JWST imaging, of a distant galaxy that is magnified by gravitational lensing. JWST spectroscopy of the galaxy, at rest-frame optical wavelengths, detects strong nebular emission lines that are attributable to oxygen and hydrogen. The measured redshift is $z = 9.51 \pm 0.01$, corresponding to 510 million years after the Big Bang. The galaxy has a radius of $16.2^{+4.6}_{-7.2}$ parsecs, which is substantially more compact than galaxies with equivalent luminosity at $z \sim 6$ to 8, leading to a high star formation rate surface density.

Radiation from early galaxies is thought to be responsible for the reionization of the Universe, the process in which the majority of the intergalactic neutral gas was ionized by high-energy photons. Observational constraints suggest that reionization was completed when the Universe was approximately 1 billion years old (redshift $z \sim 6$) (*1*). The precise timeline of reionization, and the relative contributions of faint and bright galaxies to the ionizing photon budget, remain uncertain (*2*). Observations of distant galaxies that existed during the epoch of reionization provide information on the physical processes that occurred during that period (*3*).

The intrinsic faintness and small angular sizes of galaxies at high redshift limit our ability to observe them in detail. Because of their very large masses, galaxy clusters act as gravitational lenses, magnifying the flux and stretching the angular extent of distant background galaxies. Gravitational lensing can therefore extend the observational limits of a telescope, probing faint and small galaxies at high redshifts that would otherwise be undetectable (*4*).

Near-infrared imaging has identified distant galaxy candidates at redshift $z \gtrsim 9$ and up to $z \simeq 17$ (*5–7*), but the redshifts of those candidates have not been confirmed with spectroscopy. Among these candidates are an unexpectedly large number of galaxies with bright ultraviolet (UV) absolute magnitudes ($M_{\rm UV} \lesssim -21$ mag) (*8–10*) and high stellar masses [$M_* > 10^{10}$ solar masses ($M_\odot$)] (*11*). This population was not predicted by simulations of early galaxy formation that assumed standard cosmology (*12*, *13*). Spectroscopy is necessary to confirm the redshifts of these galaxies and infer their physical properties, from the strengths of their emission lines.

Nebular emission lines are produced by clouds of interstellar gas within a galaxy; spectroscopic analysis of these lines can provide information about the density, temperature, and chemical composition of the gas. Spectroscopy has confirmed three high-redshift galaxies ($7.66 < z < 8.50$) with detections of strong nebular emission lines (*14*) and the temperature-sensitive [O III] 4363 Å emission line, which has been used to make direct electron temperature oxygen abundance measurements in galaxies at these redshifts (*15–19*). There has been further spectroscopic confirmation of seven galaxies from $z = 7.762$ to 8.998 (*20*).

## Imaging observations and analysis

We observed the galaxy cluster RX J2129.6+0005 (hereafter RX J2129) on 6 October 2022 using the Near-Infrared Camera (NIRCam) ins ment on JWST, operating in imaging mode as part of a director's discretionary time program (number DD 2767; principal investigator, P. Kelly). NIRCam is sensitive to wavelengths in the range of 0.6 to 5.0 μm; we obtained exposures in the F115W, F150W, F200W, F277W, F356W, and F444W filters (the name of each filter indicates its approximate central wavelength and bandwidth; for example, the central wavelength of the F115W filter is ~1.15 μm and has a wide bandwidth of 0.225 μm). Our exposure times ranged from 2026 s for the F444W filter to 19,927 s for the F150W filter. The astrometric alignment for the NIRCam images was performed by using a catalog prepared from previous imaging taken with the Suprime-Cam instrument on the Subaru telescope (*21*).

The color-composite NIRCam image of the RX J2129 cluster is shown in Fig. 1. In this image, we identified a candidate distant galaxy (which we designate as RX J2129-z95), which appears as three images because of the gravitational lensing of the foreground cluster. Coordinates for the three images—designated RX J2129-z95:G1, RX J2129-z95:G2, and RX J2129-z95:G3 (hereafter G1, G2 and G3)—are given in table S2. Photometric measurements from the NIRCam imaging, along with measurements from previous Hubble Space Telescope (HST) imaging of the RX J2129 cluster field obtained with the Advanced Camera for Surveys (ACS) and the Wide Field Camera 3 (WFC3), are listed in table S1 (*21*).

We used the EAZY-PY software (*22*) to constrain the photometric redshift (an estimate for a source's redshift made without the use of spectroscopy) for all sources in the field detected in the NIRCam imaging (*21*). We obtained a photometric redshift of $z_{\rm phot} = 9.38^{+0.29}_{-0.15}$ for image G2 of RX J2129-z95. From the NIRCam photometry, we estimated a UV spectral slope (β) of $-1.98 \pm 0.11$ (*21*). Using the F150W photometric flux measurement, and correcting for the effect of magnification from gravitational lensing of image G2 (magnification $\mu = 20.2 \pm 3.8$) (*21*), we calculated the absolute UV magnitude at 1500 Å $M_{\rm UV} = -1.72 \pm 0.22$ mag.

We used the PROSPECTOR software (*23*) to infer the physical properties of the galaxy from the spectral energy distribution (SED) of image G2, using the NIRCam photometry and nondetections from archival optical HST imaging (*21*). Before doing so, we corrected the photometry for the effect of magnification from gravitational lensing. We found that the galaxy has a low stellar mass $\log(M_*/M_\odot) = 7.63^{+0.22}_{-0.24}$ (uncertainty is 1σ and includes the propagated uncertainty in magnification). The template fitting also indicates an oxygen abundance of $12 + \log({\rm O/H}) = 7.63^{+0.07}_{-0.05}$. The best-fitting star formation history (SFH) has a mass-weighted age of $56^{+43}_{-34}$ million years

---

[1] Minnesota Institute for Astrophysics, University of Minnesota, Minneapolis, MN 55455, USA. [2] Cosmic Dawn Center, Niels Bohr Institute, University of Copenhagen, DK-2200 Copenhagen, Denmark. [3] Physics Department, Ben-Gurion University of the Negev, Beer-Sheva 8410501, Israel. [4] Department of Physics and Astronomy, University of California, Los Angeles, CA 90095, USA. [5] Space Telescope Science Institute, Baltimore, MD 21218, USA. [6] Center for Frontier Science, Chiba University, Chiba 263-8522, Japan. [7] Department of Physics, Chiba University, Chiba 263-8522, Japan. [8] Instituto de Física de Cantabria, Universidad de Cantabria, Consejo Superior de Investigaciones Científicas, 39005 Santander, Spain. [9] Istituto Nazionale di Astrofisica, Osservatorio Astronomico di Trieste, 34124 Trieste, Italy. [10] Dark Cosmology Center, Niels Bohr Institute, University of Copenhagen, DK-2200 Copenhagen, Denmark. [11] Donostia International Physics Center, Ikerbasque Foundation, University of the Basque Country, 20018 Donostia, Spain. [12] Instituto de Astrofisica de Canarias, E-38205 La Laguna, Tenerife, Spain. [13] Departamento de Astrofísica, Universidad de La Laguna, 38206 La Laguna, Tenerife, Spain. [14] Department of Astronomy and Astrophysics, University of California Observatories/Lick Observatory, University of California, Santa Cruz, CA 95064, USA. [15] Department of Physics and Astronomy, Rutgers, The State University of New Jersey, Piscataway, NJ 08854, USA. [16] Department of Astronomy, University of California, Berkeley, CA 94720-3411, USA. [17] Kavli Institute for the Physics and Mathematics of the Universe, The University of Tokyo, Kashiwa 277-8583, Japan.
***Corresponding author. Email: will5099@umn.edu**

and indicates a star formation rate (SFR) of SFR = 0.9 ± 0.32 $M_\odot$ year$^{-1}$. The observed SED of image G2 and best-fitting Prospector model are shown in fig. S3.

We used the Lenstruction software (*24*, *25*) to reconstruct the F150W image of G2, correcting for the effects of gravitational lensing and the NIRCam point spread function (PSF). We fitted the reconstructed image with a surface brightness model, which consisted of an elliptical Sèrsic profile with index $n$ fixed to 0.5 ($n$ determines the degree of curvature of the profile, with $n$ = 0.5 being a Gaussian profile). This indicates that the intrinsic half-light radius of the reconstructed source is $R_{\mathrm{e,intrinsic}} = 16.2^{+4.6}_{-7.2}$ pc (fig. S7). We also fitted the observed F150W image directly, using the Galight software (*26*), which indicates an observed angular size of $\theta_{\mathrm{e,observed}}$ = 0.04 ± 0.01 arc sec (*21*).

### Spectroscopic observations and analysis

We obtained follow-up spectroscopy of the RX J2129 cluster field on 22 October 2022, using JWST's Near Infrared Spectrograph (NIRSpec) in multiobject spectroscopy (MOS) mode. Targets were selected on the basis of photometric redshift estimates from the NIRCam imaging. We used a standard three-shutter dither pattern and obtained a 4464-s exposure using the prism disperser. This setup provides wavelength coverage from 0.6 μm to 5.3 μm, with spectral resolving power $R$ ranging from ≈50 to ≈400 (*27*). The fully calibrated (*21*) one-dimensional (1D) and 2D spectra are shown in Fig. 2.

We estimated the spectroscopic redshift of the galaxy through visual identification of the emission lines Hβ and [O iii] 4959,5007 Å. We refined our redshift measurement by modeling the emission-line profiles, which yielded $z_{\mathrm{spec}}$ = 9.51 ± 0.01. This spectroscopic redshift is consistent with the photometric redshift derived previously ($z_{\mathrm{phot}} = 9.38^{+0.29}_{-0.15}$), indicating that the lines were not misidentified.

To constrain the fluxes of the emission lines, we used the pPXF (Penalized Pixel-Fitting) software (*28*), which models the stellar continuum and fits Gaussian profiles to each of the emission lines (*21*). Our measured emission-line fluxes, equivalent widths (EWs), and corresponding uncertainties are listed in Table 1. We did not detect the Lyα line of hydrogen, with a 3σ upper limit for its flux of ~39 × 10$^{-19}$ erg s$^{-1}$ cm$^{-2}$ (*21*). We assumed negligible extinction from dust and applied no reddening correction to the flux measurements (*21*).

We inferred the SFR of the galaxy from our Hβ flux measurement using the relation

$$\mathrm{SFR}/\left(M_\odot \mathrm{year}^{-1}\right) = 5.5 \times 10^{-42} L(\mathrm{H}\alpha)/\left(\mathrm{erg\ s}^{-1}\right) \quad (1)$$

where $L$(Hα) is the intrinsic Hα luminosity of the galaxy. To compute $L$(Hα), we corrected

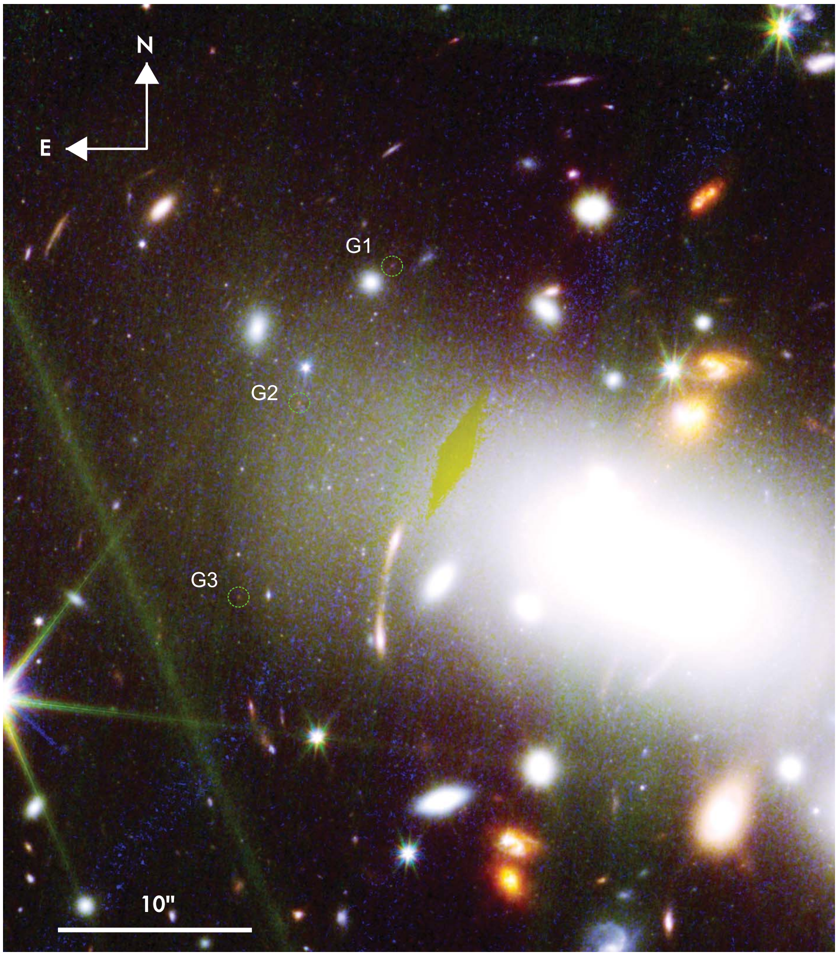

**Fig. 1. Color-composite image of part of RX J2129.** JWST NIRCam + HST ACS color-composite image of galaxy cluster RX J2129, with three images of the $z$ = 9.51 galaxy circled in green. We obtained spectroscopy of image G2. Filters were assigned to RGB colors as red, JWST F277W+F356W+F444W; green, JWST F115W +F150W+F200W; and blue, HST F606W + F814W. The broad blue and green bands are diffraction spikes caused by foreground stars. The yellow diamond is an artifact caused by a chip gap in the HST ACS camera. The individual red, green, and blue images are shown in figs. S11 to S13.

**Table 1. Emission line flux measurements.** Flux measurements and rest frame EWs of emission lines for the $z$ = 9.51 galaxy. The flux measurements have not been corrected for magnification due to gravitational lensing. Upper limits are 3σ.

| Emission line | Rest frame wavelength (Å) | Observed flux ($10^{-19}$ erg s$^{-1}$ cm$^{-2}$) | Rest frame EW (Å) |
|---|---|---|---|
| Lyα | 1216 | <39 | <31 |
| C iii] + [C iii] | 1907, 1909 | <20 | <51 |
| [O ii] | 3626, 3629 | 5.9 ± 1.6 | 44 ± 12 |
| [Ne iii] | 3869 | 6.3 ± 1.4 | 53 ± 12 |
| [Ne iii] + Hε | 3968, 3970 | <4.9 | <39 |
| Hδ | 4102 | 5.7 ± 1.2 | 52 ± 11 |
| Hγ | 4340 | 11.8 ± 1.7 | 195 ± 27 |
| [O iii] | 4363 | <5.0 | <74 |
| Hβ | 4861 | 17.8 ± 2.5 | 248 ± 35 |
| [O iii] | 4959 | 26.3 ± 1.8 | 392 ± 27 |
| [O iii] | 5007 | 79.0 ± 2.0 | 1092 ± 28 |

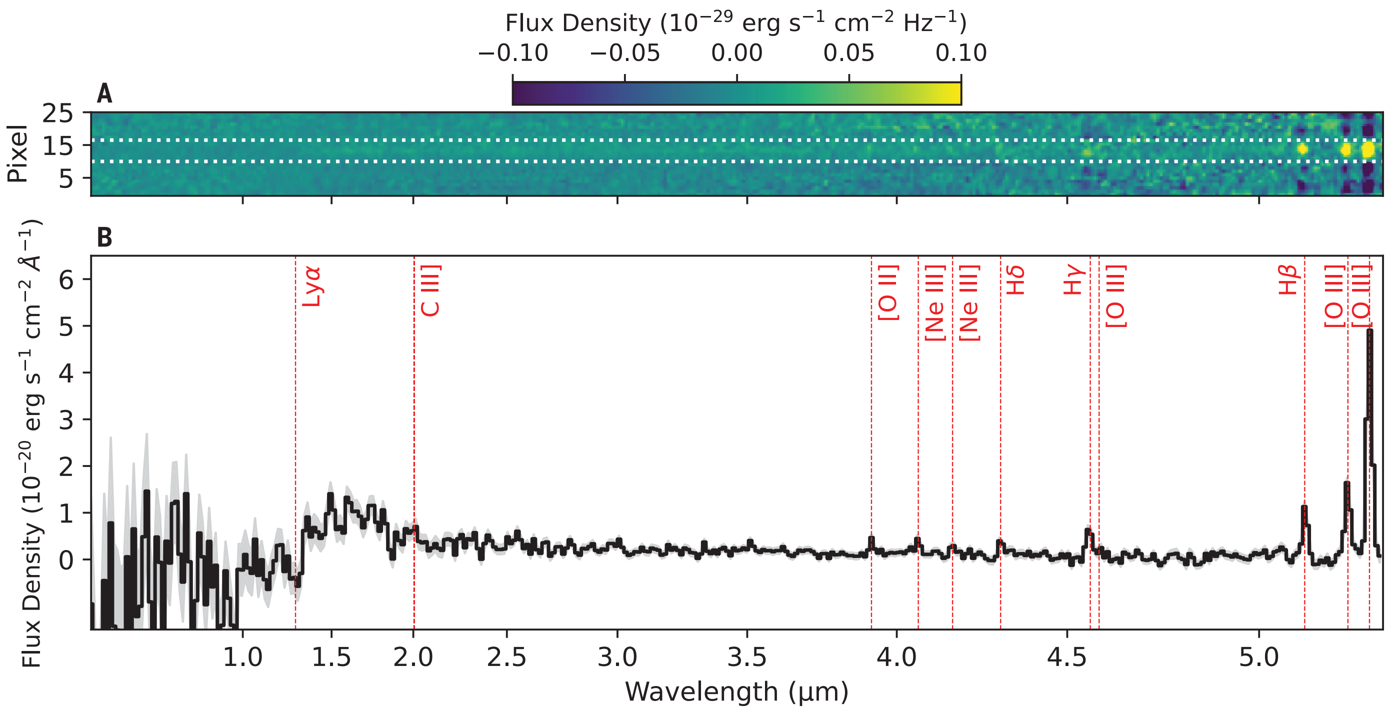

**Fig. 2. Observed JWST spectrum of image G2.** NIRSpec prism spectrum of image G2 of the $z$ = 9.51 galaxy. This spectrum has not been corrected for magnification from gravitational lensing. (**A**) Two-dimensional spectrum, with flux densities indicated by the color bar. The apparent negative fluxes, in the background near the emission lines, are artifacts produced by the dither pattern used for the NIRSpec observations. The white dotted lines indicate the window used to extract the spectrum in (B). (**B**) One-dimensional spectrum. The black line is the data, with gray shading indicating its 1σ uncertainties. Red vertical lines indicate the expected wavelengths of emission lines for $z$ = 9.51.

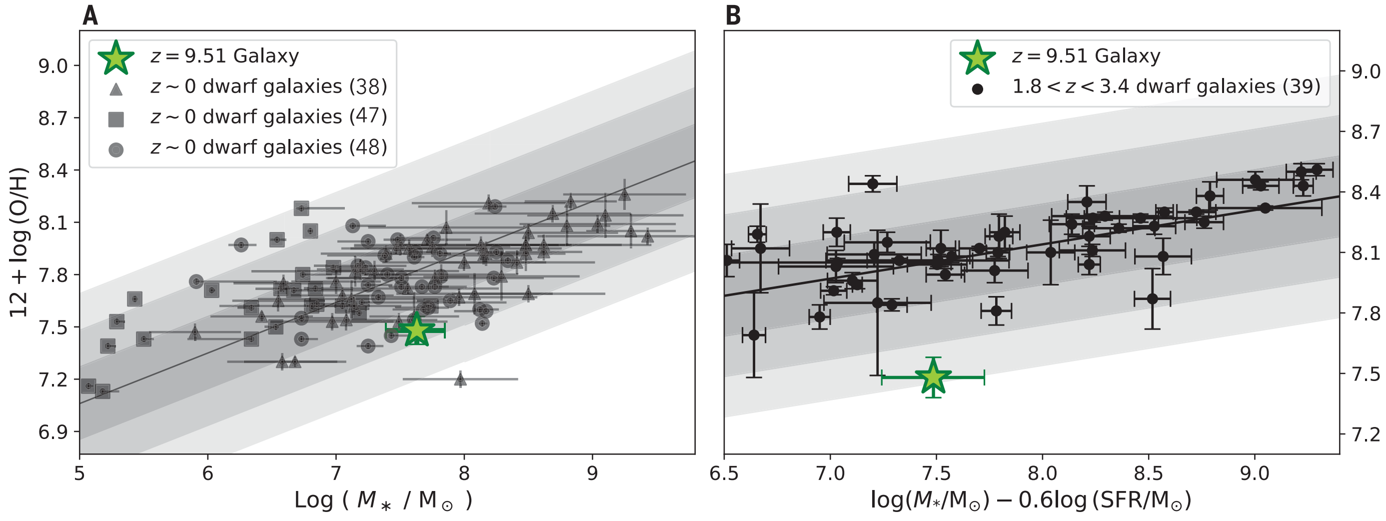

**Fig. 3. Metallicity relations.** (**A**) The $z$ = 9.51 galaxy (green star) compared with the mass-metallicity relation defined by local dwarf galaxies. Samples of local dwarfs are shown as black points (*38*, *47*, *48*), with error bars indicating 1σ uncertainties. The solid line is the mass-metallicity relation fitted to the triangle data points. Gray shading indicates, from dark to light, the 1σ, 2σ, and 3σ uncertainty ranges of this relation. (**B**) The more general fundamental metallicity relation (FMR) derived for dwarf galaxies at $z$ ~ 2 to 3 (*39*). Plotting symbols are the same as (A). The $z$ = 9.51 galaxy falls 2.5σ below this relation.

for magnification from lensing and assumed Case B recombination (*29*). We found SFR = $1.69^{+0.51}_{-0.34}$ $M_\odot$ year$^{-1}$ (*21*). This value is ~50% larger than the value we derived above from the SED (0.90 ± 0.32 $M_\odot$ year$^{-1}$), but the discrepancy is <2σ. Using the stellar mass that we inferred from the SED [$\log(M_*/M_\odot) = 7.63^{+0.22}_{-0.24}$], we computed the specific SFR (sSFR; the SFR per unit mass) and found log(sSFR) = −7.38 ± 0.26 year$^{-1}$.

To test for a spatial offset between the nebular emission and the stellar continuum, we extracted profiles along the spatial axis of the NIRSpec MOS slit. We extracted spatial profiles of the strong emission lines in 0.05-μm windows. For the stellar continuum, we extracted the spatial profile of the spectrum at all wavelengths above 1.5 μm, masking out the regions within 0.05 μm of any strong emission lines. We found no evidence for an offset between the nebular emission lines and stellar continuum (fig. S6).

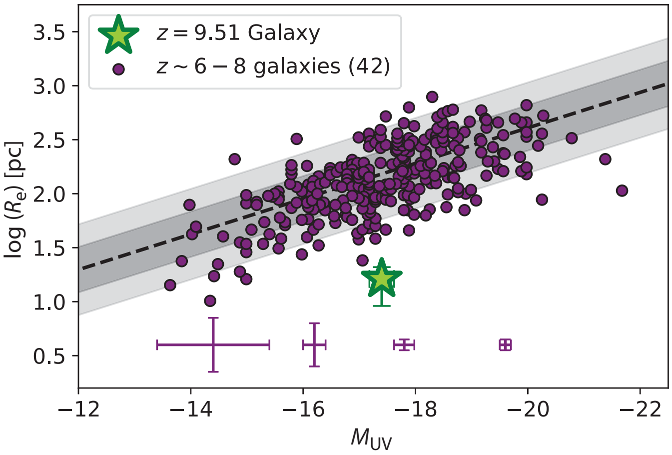

**Fig. 4. Size-luminosity relation.** The $z$ = 9.51 galaxy (green star) compared with galaxies at redshifts $z \simeq 6$ to 8 [purple circles (*42*)]. The half-light radius of the $z$ = 9.51 galaxy is a factor of $9.3^{+10.5}_{-4.4}$ (3.5σ) smaller than the size-luminosity relation fitted to the purple points (*42*) (dashed line, with dark and light gray shaded regions indicating its 1σ and 2σ uncertainty ranges). The purple error bars indicate the typical 1σ uncertainties for the $z \simeq 6$ to 8 galaxies at representative values of $M_{\rm UV}$.

We used the fluxes of the strongest emission lines of oxygen and hydrogen to estimate the oxygen abundance of the $z$ = 9.51 galaxy. The high ratio $O_{32} \equiv F([\text{O III}])/F([\text{O II}]) = 13 \pm 4$ that we calculated for this galaxy is consistent with highly ionized gas with low metallicity. We therefore used an empirical calibration (*30*) measured from low-metallicity $[12 + \log(\text{O/H}) \lesssim 8.0]$ galaxies

$$12 + \log(\text{O/H}) = 0.950\log(R_{23} - 0.08O_{32}) + 6.805 \quad (2)$$

where $R_{23} \equiv [F([\text{O II}]3727\ \text{Å}) + F([\text{O III}]4959\ \text{Å}) + F([\text{O III}]5007\ \text{Å})]/F(\text{H}\beta)$. For the $z$ = 9.51 galaxy, we found an oxygen abundance of 12 + log(O/H) = 7.48 ± 0.08, where the uncertainty includes both line-flux and calibration uncertainties (*21*). Using alternative calibrations (*31*, *32*) resulted in consistent estimates. The oxygen abundance derived from the photometry is also consistent (within 1.5σ) with the emission line calibrations (*21*).

## Galaxy properties in context

The high magnification provided by gravitational lensing enabled us to detect this intrinsically faint galaxy ($M_{\rm UV,1500} = -17.4 \pm 0.22$ mag), which has strong emission lines. Without lensing magnification, the galaxy's apparent magnitudes would be too faint to detect in the JWST images. We measured a lower mass and luminosity than those of other galaxies with strong emission line detections at $z > 7$, but a similar sSFR (fig. S4).

Star-forming galaxies that have emission lines with very large EWs at $z \lesssim 2.5$ exhibit tight correlations between the EW of the [O III] 5007 Å emission line and the $O_{32}$ ratio, and between the EWs of [O III] 5007 Å and Hβ (*33*). The properties of the $z$ = 9.51 galaxy are consistent with both of these relations within 2σ (fig. S5). The high $O_{32}$ = 13 ± 4 we measured for this object is similar to that of other galaxies with high EW emission lines at high redshifts during the epoch of reionization, and of their local counterparts (*34*, *35*). The high $O_{32}$ might indicate a high escape fraction of hydrogen-ionizing radiation, $f_{\rm esc}$. For example, using an empirical relation (*36*), we inferred $f_{\rm esc}$ = 0.65 ± 0.45. However, there is large scatter in this relation, and other methods of inferring $f_{\rm esc}$ do not yield such high escape fractions. For example, the UV spectral slope (β = −1.98 ± 0.11) suggests a much smaller escape fraction, $f_{\rm esc}$ = 0.035 ± 0.011 (*37*). Given these discrepant indicators and large uncertainties, we cannot draw any conclusions about $f_{\rm esc}$ from this galaxy.

The oxygen abundance is 12 + log (O/H) = 7.48 ± 0.08, which is consistent (within 2σ) with the mass-metallicity relation observed in the local Universe for similar-mass galaxies (*38*). The galaxy's oxygen abundance is ~0.6 dex less (2.5σ) than the more general relation between stellar mass, SFR, and metallicity [the fundamental metallicity relation (FMR)] for dwarf galaxies at $z \sim 2$ to 3 (Fig. 3) (*39*). The oxygen abundances at redshift $z \gtrsim 3$ are known to fall below the FMR by 0.3 to 0.6 dex (*40*).

To determine whether the $z$ = 9.51 galaxy hosts an active galactic nucleus (AGN), we compared our measurements of the stellar mass and the [O III] 5007 Å with Hβ emission-line flux ratio {log[$F$([O III])/$F$(Hβ)] = 0.65 ± 0.06} with measurements from a sample of local galaxies at redshifts $0.04 < z < 0.2$ (*41*). At stellar masses and emission line ratios similar to those of the $z$ = 9.51 galaxy, <1% of the local galaxies were classified as AGN. If this fraction does not substantially evolve with redshift, it is unlikely that the $z$ = 9.51 galaxy hosts an AGN.

The half-light radius we measured for this galaxy, $R_e = 16.2^{+4.6}_{-7.2}$ pc, is very compact compared with that of galaxies with similar luminosities at redshifts $z \simeq 6$ to 8 (Fig. 4). The half-light radius of the $z$ = 9.51 galaxy is a factor of $9.8^{+6.5}_{-2.6}$ times smaller than the size-luminosity relation at those redshifts (*42*)—a 4σ difference. The galaxy is also more compact than individual star-forming clumps with similar SFRs observed at redshifts $1 < z < 8$ (fig. S9) (*43*). Star-forming clumps have been shown to have a trend of increasing SFR at a fixed size with increasing redshift (*44*).

From our measurements of the SFR and half-light radius of the galaxy, we infer a very high SFR surface density $\sum_{\rm SFR} 1190^{+2440}_{-580}\ M_\odot$ year$^{-1}$ kpc$^{-2}$. $\Sigma_{\rm SFR}$ has been observed to increase with redshift from $z \sim 0$ to ~8 (*45*). The $\Sigma_{\rm SFR}$ of the $z$ = 9.51 galaxy is a factor of $38^{+129}_{-11}$ times greater than that of the galaxies in the highest redshift bin ($z \sim 8$) of that sample (fig. S8).

## REFERENCES AND NOTES

1. N. Aghanim *et al.*, *Astron. Astrophys.* **641**, A6 (2020).
2. S. L. Finkelstein *et al.*, *Astrophys. J.* **879**, 36 (2019).
3. P. Dayal, *Proc. Int. Astron. Union* **15** (S352), 43–43 (2019).
4. B. E. Robertson *et al.*, *Astrophys. J.* **768**, 71 (2013).
5. N. J. Adams *et al.*, *Mon. Not. R. Astron. Soc.* **518**, 4755–4766 (2022).
6. M. Castellano *et al.*, *Astrophys. J. Lett.* **938**, L15 (2022).
7. H. Yan, Z. Ma, C. Ling, C. Cheng, J.-S. Huang, *Astrophys. J. Lett.* **942**, L9 (2022).
8. H. Atek *et al.*, *Mon. Not. R. Astron. Soc.* **519**, 1201–1220 (2022).
9. S. L. Finkelstein *et al.*, *Astrophys. J. Lett.* **940**, L55 (2022).
10. R. P. Naidu *et al.*, *Astrophys. J. Lett.* **940**, L14 (2022).
11. I. Labbé *et al.*, *Nature* **616**, 266–269 (2023).
12. C. A. Mason, M. Trenti, T. Treu, *Mon. Not. R. Astron. Soc.* **521**, 497–503 (2023).
13. M. Boylan-Kolchin, arXiv:2208.01611 [astro-ph.CO] (2022).
14. A. C. Carnall *et al.*, *Mon. Not. R. Astron. Soc. Lett.* **518**, L45–L50 (2022).
15. K. Z. Arellano-Córdova *et al.*, *Astrophys. J. Lett.* **940**, L23 (2022).
16. M. Curti *et al.*, *Mon. Not. R. Astron. Soc.* **518**, 425–438 (2022).
17. J. E. Rhoads *et al.*, *Astrophys. J. Lett.* **942**, L14 (2023).
18. D. Schaerer *et al.*, *Astron. Astrophys.* **665**, L4 (2022).
19. J. R. Trump *et al.*, *Astrophys. J.* **945**, 35 (2023).
20. S. Fujimoto *et al.*, arXiv:2301.09482 [astro-ph.GA] (2023).
21. Materials and methods are available as supplementary materials.
22. G. B. Brammer, P. G. van Dokkum, P. Coppi, *Astrophys. J.* **686**, 1503–1513 (2008).
23. B. D. Johnson, J. Leja, C. Conroy, J. S. Speagle, *Astrophys. J. Suppl. Ser.* **254**, 22 (2021).
24. L. Yang, S. Birrer, T. Treu, *Mon. Not. R. Astron. Soc.* **496**, 2648–2662 (2020).
25. S. Birrer *et al.*, *J. Open Source Softw.* **6**, 3283 (2021).
26. X. Ding, S. Birrer, T. Treu, J. D. Silverman, arXiv:2111.08721 [astro-ph.GA] (2021).
27. P. Jakobsen *et al.*, *Astron. Astrophys.* **661**, A80 (2022).
28. M. Cappellari, arXiv:2208:14974 [astro-ph.GA] (2022).
29. D. E. Osterbrock, *Astrophysics of Gaseous Nebulae and Active Galactic Nuclei* (University Science Books, 1989).
30. Y. I. Izotov, N. G. Guseva, K. J. Fricke, C. Henkel, *Astron. Astrophys.* **623**, A40 (2019).
31. R. Maiolino *et al.*, *Astron. Astrophys.* **488**, 463–479 (2008).
32. T. Jiang, S. Malhotra, J. E. Rhoads, H. Yang, *Astrophys. J.* **872**, 145 (2019).
33. M. Tang, D. P. Stark, J. Chevallard, S. Charlot, *Mon. Not. R. Astron. Soc.* **489**, 2572–2594 (2019).
34. N. R. Eggen, C. Scarlata, E. Skillman, A. Jaskot, *Astrophys. J.* **912**, 12 (2021).
35. S. R. Flury *et al.*, *Astrophys. J. Suppl. Ser.* **260**, 1 (2022).
36. Y. I. Izotov *et al.*, *Mon. Not. R. Astron. Soc.* **474**, 4514–4527 (2018).
37. J. Chisholm *et al.*, *Mon. Not. R. Astron. Soc.* **517**, 5104–5120 (2022).
38. Y.-H. Lin *et al.*, arXiv:2211.02094 [astro-ph.GA] (2022).
39. M. Li *et al.*, arXiv:2211.01382 [astro-ph.GA] (2022).
40. P. Troncoso *et al.*, *Astron. Astrophys.* **563**, A58 (2014).

41. S. Juneau *et al*., *Astrophys. J.* **788**, 88 (2014).
42. R. J. Bouwens *et al*., *Astrophys. J.* **927**, 81 (2022).
43. A. Claeyssens *et al*., *Mon. Not. R. Astron. Soc.* **520**, 2180–2203 (2023).
44. R. C. Livermore *et al*., *Mon. Not. R. Astron. Soc.* **450**, 1812–1835 (2015).
45. T. Shibuya, M. Ouchi, Y. Harikane, *Astrophys. J. Suppl. Ser.* **219**, 15 (2015).
46. H. Williams, Photometry and Spectroscopy of a z=9.51 galaxy in the RXJ2129 cluster field. Zenodo (2023); doi:10.5281/zenodo.7767677.
47. D. A. Berg *et al*., *Astrophys. J.* **754**, 98 (2012).
48. T. Hsyu, R. J. Cooke, J. X. Prochaska, M. Bolte, *Astrophys. J.* **863**, 134 (2018).

## ACKNOWLEDGMENTS

We thank E. Skillman, N. Eggen, and A. Criswell for very helpful comments and S. Suyu for assistance in obtaining the follow-up data. We thank program coordinator T. Royle and instrument scientists A. Rest, D. Karakala, and P. Ogle of STScI for their help carrying out the HST observations. **Funding:** P.L.K. is supported by NSF grant AST-1908823 and STScI programs GO-15936, GO-16728, and GO-17253. M.O. acknowledges support by JSPS KAKENHI grants JP20H00181, JP20H05856, JP22H01260, and JP22K21349. T.T. acknowledges the support of NSF grant AST-1906976. R.J.F is supported in part by NSF grant AST–1815935, the Gordon & Betty Moore Foundation, and a fellowship from the David and Lucile Packard Foundation. A.V.F. is grateful for financial assistance from the Christopher R. Redlich Fund. G.B. is funded by the Danish National Research Foundation (DNRF) under grant 140. A.Z. acknowledges support by grant 2020750 from the United States–Israel Binational Science Foundation (BSF) and grant 2109066 from the United States National Science Foundation (NSF), and by the Ministry of Science & Technology, Israel. J.H. and D.L. were supported by a VILLUM FONDEN Investigator grant (project number 16599). T.B. acknowledges support from the AEI under grant PID2020-114035GB-100 and the Hong Kong Collaborative Research Fund under grant C6017-20G. I.P.-F. and F.P. acknowledge support from the Spanish State Research Agency (AEI) under grant PID2019-105552RB-C43. **Author contributions:** H.W. drafted the manuscript. H.W., P.L.K., C.S., N.R., T.T., and A.V.F. revised the manuscript. W.C. reduced the spectroscopy, and H.W. analyzed the spectroscopy. C.S., Y.-H.L., N.R., T.T., W.C., D.L., A.Z, L.Y., and T.B. contributed to the interpretation. T.T., W.C., A.V.F., R.J.F., J.H., A.M.K., L.S., J.P., T.B., S.J., G.B., I.P.-F., F.P., and M.N. obtained JWST imaging. G.B. measured the photometry. M.O., A.Z., and J.M.D. modeled the gravitational lensing. **Competing interests:** We declare no competing interests. **Data and materials availability:** Raw HST imaging and JWST imaging and spectroscopy are available at https://mast.stsci.edu under Proposal IDs 02767 for JWST and 12457 for HST. Our reduced HST imaging, JWST imaging, and JWST spectroscopy are archived at (*46*). Our measured photometry is provided in Table S1 and measured line fluxes in Table 1. The raw Subaru imaging is available at https://smoka.nao.ac.jp/objectSearch.jsp by selecting Suprime-Cam, then object RXJ2129+0005.

## SUPPLEMENTARY MATERIALS

science.org/doi/10.1126/science.adf5307
Materials and Methods
Figs. S1 to S13
Tables S1 to S3
References (*49*–*83*)

Submitted 27 October 2022; accepted 28 March 2023
Published online 13 April 2023
10.1126/science.adf5307